Effect of Composition on the Solidification Behavior of Several Ni-Cr-Mo and Fe-Ni-Cr-Mo Alloys

M.J. PERRICONE and J.N. DUPONT

The microstructural development of several Ni-Cr-Mo and Fe-Ni-Cr-Mo alloys over a range of conditions has been examined. A commercial alloy, AL-6XN, was chosen for analysis along with three experimental compositions to isolate the contribution of individual alloying elements to the overall microstructural development. Detailed microstructural characterization on each alloy demonstrated that the observed solidification reaction sequences were primarily dependent on the segregation behavior of molybdenum (Mo), which was unaffected by the large difference in cooling rate between differential thermal analysis (DTA) samples and welded specimens. This explains the invariance of the amount of eutectic constituent observed in the microstructure in the welded and DTA conditions. Multicomponent liquidus projections developed using the CALPHAD approach were combined with solidification path calculations as a first step to understanding the observed solidification reaction sequences. Discrepancies between the calculations and observed reaction sequences were resolved by proposing slight modifications to the calculated multicomponent liquidus projections.

I. INTRODUCTION

THE excellent corrosion resistance of superaustenitic stainless steels (SASS) makes these materials attractive for use in aggressive environments. However, conventional arc welding processes result in the redistribution of strategic alloying elements in the fusion zone, which compromises local corrosion resistance. The tendency of molybdenum (Mo) to segregate to the interdendritic regions in the fusion zone has been well demonstrated in the technical literature,[1–3] as has the corresponding susceptibility of the solute-depleted dendrite cores to preferential corrosive attack.[4–9] To combat this phenomenon, high-Mo nickel-base filler metals such as IN622 and IN625 are often employed during conventional arc welding of SASS alloys to increase the minimum solute content in the dendrite cores.[3,10] In some cases, high energy density welding processes (laser and electron beam)[11,12] can also be used to potentially restore fusion zone corrosion resistance without the need for filler material.[13–15] This technique relies on the accurate control of solidification parameters (solidification velocity and temperature gradient) to induce dendrite tip undercooling and concomitant dendrite core enrichment, which can often be difficult in many practical applications. Furthermore, the redistribution of Mo during solidification has been shown to be largely responsible for the performance and microstructural development of this class of materials,[1,2,16–19] but previous work aimed at interpreting microstructural development for conventional stainless steels[1,19–23] is based exclusively on the Fe-Ni-Cr ternary system. As such, these interpretations must be expanded to improve the understanding of the microstructural development of SASS welds, particularly in describing solute redistribution and resultant fusion zone microstructure as a function of composition in this alloy system. To that end, the objective of this research is to characterize the effect of multicomponent alloy composition on overall microstructural development in order to provide an avenue for control of fusion zone properties in SASS welds.

M.J. PERRICONE, former Doctoral Student, with the Department of Materials Science and Engineering, Lehigh University, is currently a Senior Technical Staff Member, with the Joining and Coatings Division, Sandia National Laboratories, Albuquerque, NM 87185. Contact e-mail: mperric@sandia.gov J.N. DUPONT, Associate Professor, is with the Department of Materials Science and Engineering, Lehigh University, Bethlehem, PA 18015.

Manuscript submitted July 2, 2005.

II. EXPERIMENTAL PROCEDURE

A. *Experimental Alloy Preparation*

The commercially available SASS alloy chosen as the basis for this study was AL-6XN, the composition of which can be found in Table I. To isolate the contribution of individual elements, simpler experimental alloy compositions were also examined that closely simulate the solidification behavior of dissimilar welds made between AL-6XN and Ni-base filler metals.[3] Each experimental alloy was chosen to exhibit primary austenite solidification followed by the formation of a Mo-rich eutectic constituent in the interdendritic region,[24] although the amount of this eutectic was observed to vary significantly from alloy to alloy. The compositions of the alloys are also shown in Table I. Alloys 2 and 3 are basically Ni-Cr-Mo materials in which the Mo concentration of alloy 3 is approximately twice that of alloy 2. Similarly, AL-6XN and alloy 1 are essentially Fe-Ni-Cr-Mo alloys in which the Mo content of alloy 1 is about twice that of AL-6XN. Thus, the matrix provides the opportunity to observe the influence of both Mo and Fe content on the overall solidification behavior.

A 23-kg ingot of each experimental material was cast from virgin elements using a vacuum induction melting furnace. Each ingot was then rolled at ~1200 °C into 8-mm-thick plate, approximately 100-mm wide. Homogenization treatments were then conducted on each experimental alloy to reduce as much as possible any segregation that may have occurred during casting and to ensure a uniform microstructure, which was verified by microstructural analysis. Experimental alloy 1 was homogenized for 4 hours at 1204 °C, alloy 2 for 16 hours at 1204 °C, and alloy 3 for 16 hours at 1246 °C. These temperatures were selected due to their proximity to the solidus temperature for each alloy,

Table I. Chemical Compositions for Experimental Alloys (all Values in Weight Percent)

Element	AL-6XN	Experimental Alloy 1	Experimental Alloy 2	Experimental Alloy 3
Fe	46.8	43.6	0.1	0.1
Ni	24.2	23.9	66.9	54.5
Cr	21.6	20.1	20.6	20.2
Mo	6.1	12.4	12.1	24.3
Cu	0.3	—	—	—
Si	0.5	—	0.1	0.3
Mn	0.4	0.01	—	—
C	0.02	0.03	0.02	0.02
O	0.005	0.014	0.011	0.015
N	0.24	0.017	0.006	0.008

as calculated using the Thermo-Calc computational thermodynamics package[25,26] and Ni-Data database,[27] to maximize diffusivity within the material. Alloy composition of the finished plate was verified by inductively coupled plasma (ICP) spectrometry.

Single pass autogenous gas tungsten arc (GTA) welds were prepared on the surface of each alloy with the following conditions: arc current of 200 A, travel speed of 3 mm/s, and voltage of 11 V. Argon shielding gas was used and the arc length was maintained at 2.67 mm for each weld.

B. *Differential Thermal Analysis*

The temperatures of primary γ and eutectic formation during solidification were measured using differential thermal analysis (DTA) for each material in the homogenized condition. Analysis was conducted on a Netzsch STA 409 (Burlington, MA) differential thermal analyzer using samples ranging from 700 to 950 mg. Alumina (Al_2O_3) powder was used as the reference material during testing. Alloy test specimens were packed in alumina powder in small crucibles for insulation, while melting and solidification of the samples were conducted under flowing argon for protection from atmospheric interactions. Each sample was heated from room temperature at a rate of 50 °C per minute up to 1100 °C, at which point the heating rate was changed to 10 °C/min. Once the peak temperature for each alloy was reached (~20 °C above calculated liquidus), a cooling rate of 10 °C/min was used to solidify and cool the sample to 1100 °C, at which point the sample was cooled to room temperature at a rate of 50 °C/min. An exception was made for AL-6XN, for which an optimum heating and cooling rate of 5 °C/min was empirically determined to maximize the signal for eutectic formation upon cooling. Temperatures of primary and eutectic-type reactions that occurred during solidification were taken as deviations from the local baseline in a manner consistent with previous studies.[28–33]

C. *Microstructural Analysis*

Subsequent to DTA testing, one sample for each alloy was extracted from the disposable DTA testing crucibles and set aside for metallographic sample preparation. Likewise, the autogenous single-pass GTA welds were sectioned in the transverse direction, so that a cross section of the fusion zone microstructure could be observed. Each sample was mounted and metallographically prepared. All samples were electrolytically etched in a 60 pct HNO_3/40 pct H_2O solution to reveal the microstructure.

Light optical microscopy (LOM) was used to observe microstructural features in each sample. Quantitative image analysis was used to measure the area fraction of eutectic constituent, which was assumed to be equivalent to volume fraction.[34] Scanning electron microscopy (SEM) was conducted on both the GTA welded samples and the DTA specimens using a JEOL* 6300F cold field emission scanning electron microscope at 15 kV accelerating voltage and a working distance of 19 mm. Collection of higher resolution images of eutectic morphologies was completed along with qualitative chemical analysis using energy dispersive spectroscopy.

*JEOL is a trademark of Japan Electron Optics Ltd., Tokyo.

Electron probe microanalysis (EPMA) was conducted using a JEOL 733 Superprobe equipped with four independent wavelength dispersive spectrometers. The EPMA was completed using an accelerating voltage of 15 kV and a beam current of 32 nA. The K_α lines were used for elements Fe, Ni, and Cr, while the L_α line was used for Mo.[24] Raw data were converted to weight percentages using an established ZAF algorithm.[35] Phase identification was completed using a JEOL 2010F transmission electron microscope (TEM, 200 kV accelerating voltage) to obtain selected area diffraction patterns at a high symmetry zone axis. Thin foil specimens were prepared directly from metallographic samples using the focused ion beam technique on an FEI Strata DB 235 (Hillsboro, OR). Samples were selected from very specific regions of the microstructure and ion milled to electron transparency *in situ* before being removed and placed on a TEM grid.

III. RESULTS AND DISCUSSION

A. *Microstructural Characterization*

The microstructures of the DTA samples from AL-6XN and the three experimental alloys are generally composed of coarse primary γ dendrites with varying amounts of eutectic forming in the interdendritic regions, as shown in Figure 1. The corresponding DTA scans under a 10 °C/min cooling rate are displayed in Figure 2. The cooling curve for AL-6XN (Figure 2(a)) exhibits primary austenite solidification at 1403 °C before the formation of a terminal eutectic constituent at 1354 °C. Alloy 1, a Fe-base quaternary alloy with composition similar to AL-6XN but with double the Mo content, contains much more eutectic constituent (shown in Figure 1(b)), and, as a result, exhibits a much larger exothermic reaction detected in the cooling DTA scan at 1346 °C (Figure 2(b)). However, as shown in Figure 1(c), the etched microstructure of Ni-based alloy 2 (same nominal Mo and Cr content as alloy 1) exhibits a primary γ dendritic substructure with no evidence of eutectic formation in the interdendritic regions. The corresponding DTA cooling scan (Figure 2(c)) confirms the lack of second-phase microstructural constituent, as only a single deviation from the local baseline is observed. However, doubling the Mo content of the material in Ni-based alloy

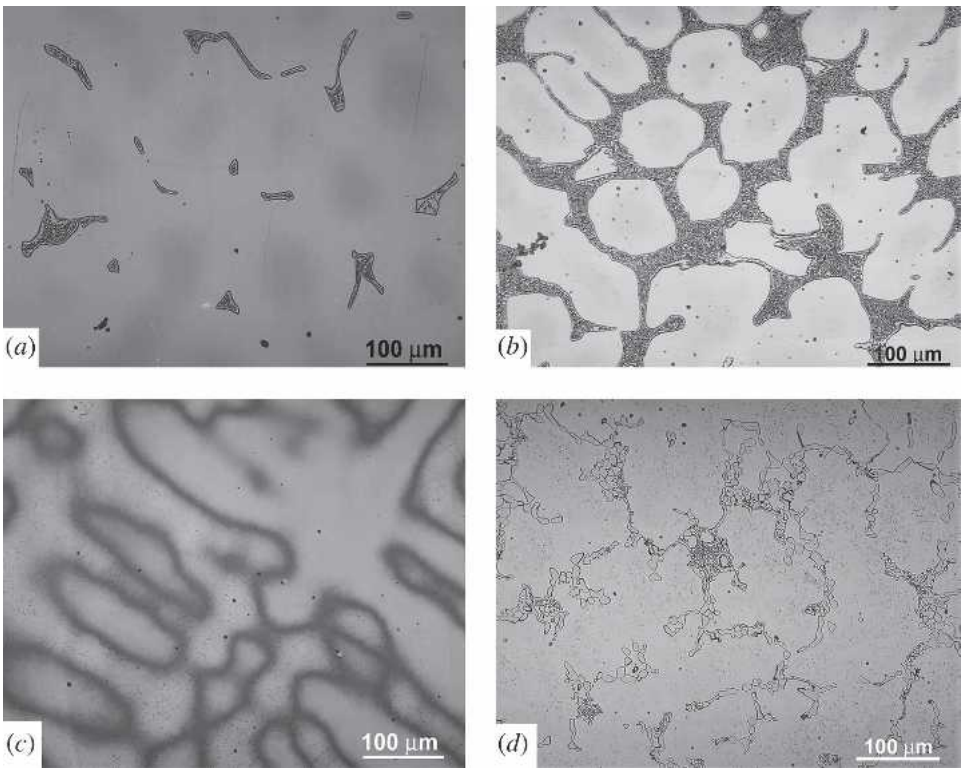

Fig. 1—Resultant microstructures for DTA of (*a*) AL-6XN, (*b*) Fe-based alloy 1, (*c*) Ni-based alloy 2, and (*d*) Ni-based alloy 3.

3 (24.3 wt pct) promotes the formation of a eutectic constituent, as shown in Figure 1(d). Further evidence of this is the secondary reaction peak at 1296 °C in the DTA scan for this alloy (Figure 2(d)).

The temperatures corresponding to the onset of primary solidification and eutectic formation as recorded during the cooling scans of the DTA experiments for AL-6XN and the three experimental alloys are shown in Table II. All values presented are averages of the duplicate runs for each material (two separate samples) to ensure reproducibility of results. While analysis of the weld fusion zone microstructures of each alloy (Figure 3) revealed a refinement in the scale of the microstructure, little appreciable difference in fraction eutectic was qualitatively observed for any of the materials, despite the large difference in cooling rate.

The SEM images of the eutectic constituents observed in the DTA specimens for each alloy are shown in Figure 4. The eutectic constituents are composed of Mo-rich intermetallics (as determined by selected area diffraction and EPMA results detailed in Sections B and C) and islands of γ-austenite. In the Fe-base alloys (Figures 4(a) and (b)), the eutectic constituents generally have similar morphologies, and the presence of a lamellar morphology (left and upper right of Figure 4(b)) was observed in alloy 1. It is anticipated that observation of these alloys in different orientations may provide evidence of areas of lamellar structure in AL-6XN as well. The eutectic constituent observed in Ni-base alloy 3 has a marginally different appearance (Figure 4(c)), suggesting the presence of a different intermetallic phase than that observed in the Fe-base alloys. The similarities and differences between the eutectic morphologies are further demonstrated by observation of the eutectic constituents present in the weld fusion zone microstructure of these alloys, as shown in Figure 5.

Electron probe microanalysis was used to experimentally measure second-phase and average eutectic compositions, as shown in Table III. In all cases, the second phase has higher Mo and Cr content than the γ matrix, typical of the intermetallic phases (σ, P, μ) that have been observed elsewhere in this class of materials.[16,36] The phase classifications used in this table are based on experimental results presented in Section B. The corresponding average eutectic compositions were also experimentally measured by leaving the electron microprobe in raster mode during the analysis,[28,33] thereby including the γ component of the eutectic constituent, which resulted in a lower average concentration of Mo and Cr and higher concentrations of Fe and Ni. The refined microstructure of the arc-welded specimens limited EPMA to measure only average compositions of the islands of eutectic ($\sim$2-μm diameter) in alloys 1 and 3. No areas of eutectic constituent larger than the minimum interaction volume of the electron probe ($\sim$1 μm) were observed in AL-6XN. However, reasonable agreement is observed between the average eutectic compositions for DTA and weld specimens for alloys 1 and 3 (as shown in Table III), strongly suggesting that the identity of the intermetallic/γ eutectic constituent did not change with cooling rate in the range studied here for each material.

B. *Phase Identification and Solidification Reactions*

The Fe-Ni-Cr-Mo and Ni-Cr-Mo alloy systems contain several intermetallic phases that can be differentiated by both chemical composition and crystal structure. Based

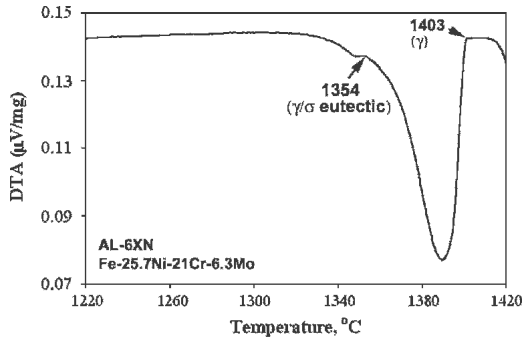

(*a*)

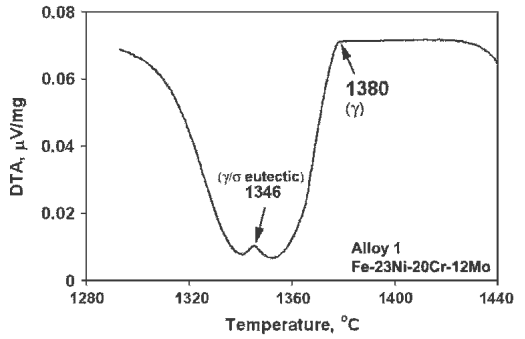

(*b*)

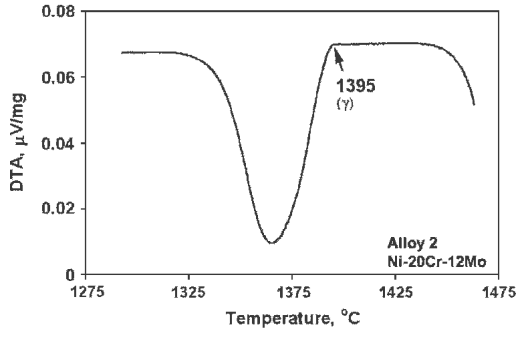

(*c*)

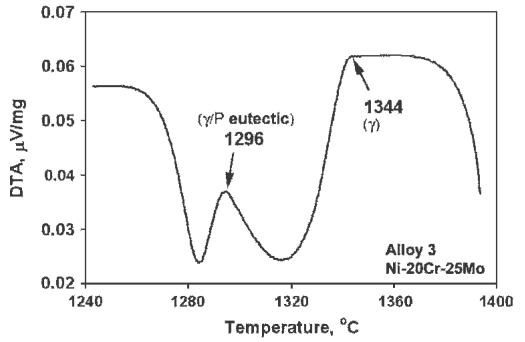

(*d*)

Fig. 2—On-cooling DTA results for (*a*) AL-6XN, (*b*) Fe-based Alloy 1, (*c*) Ni-based Alloy 2, and (*d*) Ni-based Alloy 3. Heating and cooling rates were controlled at 10 °C/min with the exception of AL-6XN (5 °C/min).

on the compositional data presented here, the possible phases in the microstructures observed in this study are γ (fcc, $a = b = c = 3.591$ Å), σ (tetragonal, $a = b = 9.08$ Å, $c = 4.75$ Å),[16] and P (orthorhombic, $a = 9.08$ Å, $b = 16.98$ Å, $c = 4.75$ Å).[16] Other studies[16,37,38] in the Ni-Cr-Mo ternary system have also reported the presence of a μ phase (hexagonal, $a = 4.76$ Å, $c = 25.91$ Å), which is postulated to be the product of a solid-state transformation from the P phase.

Table II. Critical Temperature for AL-6XN and Experimental Alloys as Determined by DTA (Standard Deviation is Expressed in Parentheses)

Material	Primary Phase (°C)	Eutectic Formation (°C)	Temperature Range (°C)
AL-6XN	1401 (3.0)	1356 (2.0)	45 (3.0)
Alloy 1	1380 (0.0)	1347 (1.0)	33 (1.0)
Alloy 2	1394 (1.0)	—	—
Alloy 3	1344 (1.0)	1296 (1.0)	48 (1.0)

The results of selected area diffraction analysis are shown in Figure 6. Samples were tilted to a high symmetry zone axis to facilitate pattern identification and indexing based on the published lattice parameters discussed previously. Based on this analysis, the intermetallic phase in both the DTA and GTA specimens of AL6XN proved to be σ, as shown in Figure 6(a) ($[\bar{1}\bar{1}3]$ zone axis) and Figure 6(b) ([110] zone axis), respectively. This σ phase was also identified in alloy 1, as illustrated in Figure 6(c), though the orientation of the sample was at a [212] zone axis in this case. The intermetallic phase in the eutectic constituent of alloy 3, however, was revealed to be the orthorhombic P phase, as depicted in Figure 6(d) [$\bar{1}$03] at a zone axis.

From these data, the solidification reactions of each alloy can be determined, providing an opportunity to examine differences in solidification behavior due to alloy compositional variations:

$$\text{AL-6XN: } L \rightarrow L + \gamma \rightarrow L + \gamma + \sigma \rightarrow \gamma + \sigma$$
$$\text{Alloy 1: } L \rightarrow L + \gamma \rightarrow L + \gamma + \sigma \rightarrow \gamma + \sigma$$
$$\text{Alloy 2: } L \rightarrow L + \gamma \rightarrow \gamma$$
$$\text{Alloy 3: } L \rightarrow L + \gamma \rightarrow L + \gamma + P \rightarrow \gamma + P$$

C. *Elemental Segregation Behavior*

The redistribution of Fe, Ni, Cr, and Mo in the solidified structure was also observed experimentally *via* EPMA for both DTA and welded specimens, examples of which are shown in Figures 7 and 8. Figure 7(a) shows the region of the DTA microstructure for Fe-base alloy 1 in which the EPMA line scan was taken, while Figure 7(b) plots the compositions of Fe, Ni, Cr, and Mo as a function of distance across the dendritic structure. Similarly, Figure 8(a) depicts the region of the fusion zone microstructure in Ni-base alloy 3 in which an EPMA line scan was taken, and Figure 8(b) shows the resulting compositional data. In each case, the local minima in Mo composition correspond to dendrite core positions, while the local maxima correspond to the interdendritic regions. Although the nominal composition for alloy 1 has 12.4 wt pct Mo, the average dendrite core composition is around 8.6 wt pct Mo; the large amount of excess Mo rejected into the liquid during solidification results in the formation of a similarly large amount of eutectic (~30 vol pct determined by quantitative image

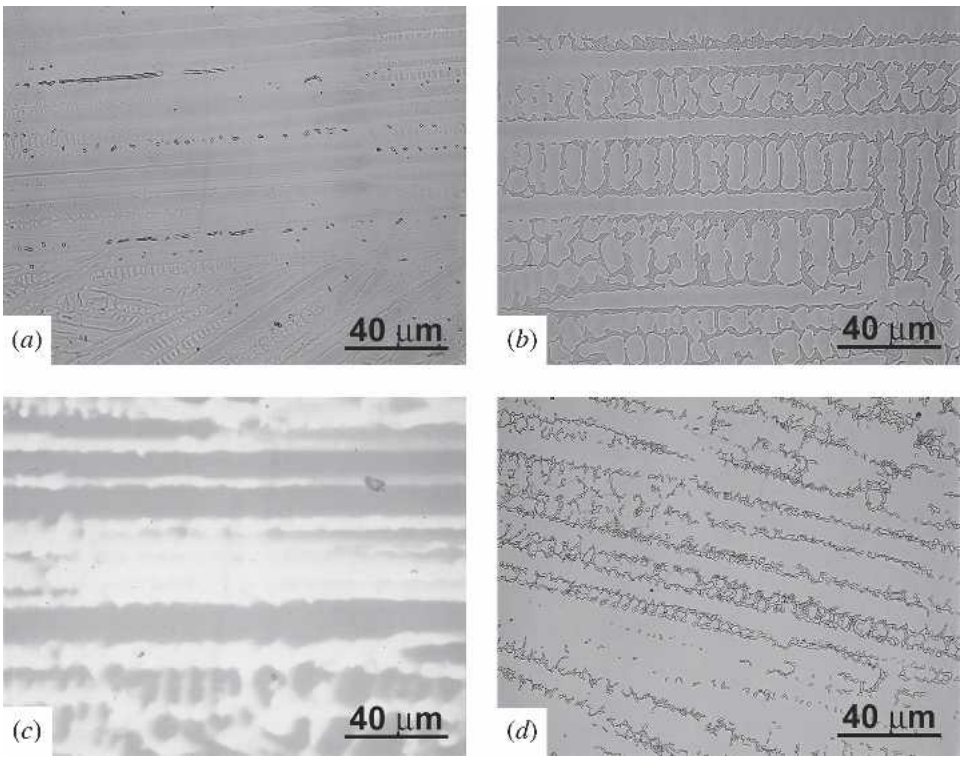

Fig. 3—Resultant microstructures for autogenous gas tungsten arc welds prepared on (*a*) AL-6XN, (*b*) Fe-based alloy 1, (*c*) Ni-based alloy 2, and (*d*) Ni-based alloy 3.

analysis). Likewise, alloy 3 has a nominal Mo composition of 24.3 wt pct though the dendrite cores exhibiting only 19.9 wt pct Mo, and a large amount of eutectic constituent (~20 vol pct) is observed. A summary of the dendrite core compositions collected *via* EPMA for each alloy is shown in Table IV; these data reflect the results of duplicate line scans in different regions of each microstructure for statistical purposes.

The dendrite core composition data can be used to experimentally determine the solute partition coefficient (k) at the start of solidification, defined at a given temperature as the ratio of solid composition to liquid composition during solidification. The dendrite core is the first solid to form as the solid-liquid interface advances, and because the diffusion of Mo in γ is known to be insignificant during solidification,[3] the core composition is assumed to be constant and can be directly measured. The liquid composition at the time the first solid forms is the nominal composition, so k at the start of solidification is simply the ratio of the dendrite core composition to the nominal composition for a given element. A summary of the measured partition coefficients for Fe, Ni, Cr, and Mo for each material is displayed in Table IV.

No significant variation in the partition coefficient measured for DTA and GTA welded specimens for each alloy was observed, indicating that the segregation behavior of Mo in these alloys is insensitive to cooling rate in the range of cooling rates studied here. It is important to note that the k value for Cr is ~1.0 for each alloy, demonstrating the low segregation potential of Cr in these alloys. Also, the tendency of Fe and Ni to segregate *to* the primary γ dendrite cores ($k > 1$) was observed for each alloy, a phenomenon that also seemed insensitive to cooling rate in the range of conditions analyzed here.

IV. INTERPRETATION OF MICROSTRUCTURAL DEVELOPMENT

A. *Multicomponent Liquidus Projections*

In an effort to understand the solidification behavior of the alloys in this study, multicomponent liquidus projections were calculated using the ThermoCalc[26] thermodynamic software combined with the Ni-Data database[27] and Fe-Data database[39] developed by ThermoTech Industries. Previous work[40] with this technique compared, with good agreement, the calculation of a ternary liquidus surface for the Ni-Cr-Mo system with a published estimated Ni-Cr-Mo liquidus projection based on experimental results.[41] These liquidus projections were combined with solidification path calculations as an aid to understanding microstructural development and the role of individual alloying elements. (It is recognized that multicomponent Scheil-type solidification calculations can be conducted directly with the Thermo-Calc program. However, as shown subsequently, the conventional method used here proved more useful for illustrating the influence of individual alloying elements on the solidification behavior.) Multicomponent liquidus projections that include varying amounts of Fe, Ni, Cr, Mo, C, Mn, Si, Cu, and N were calculated using a method similar to that demonstrated in

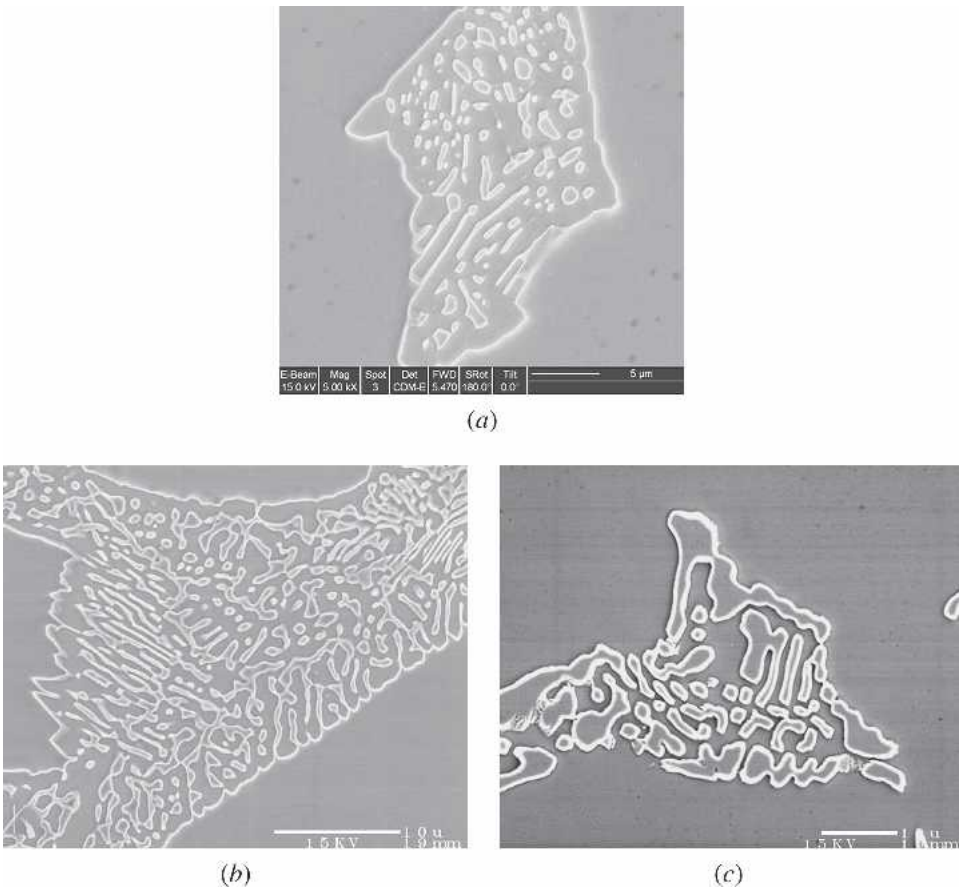

Fig. 4—Comparison of eutectic morphologies observed in a scanning electron microscope for DTA specimens: (*a*) AL-6XN exhibits eutectic with an intermetallic and γ-austenite islands, (*b*) Fe-base alloy 1 exhibits similar eutectic morphology to AL-6XN but with regions of lamellar structure, and (*c*) Ni-base alloy 3 showing a eutectic morphology with large blocky islands of intermetallic in the γ matrix. All samples are electrolytically etched with 60 pct HNO_3/40 pct H_2O mixture.

previous studies in the Fe-Ni-Cr-Mo system.[40,42] The molar fraction of the liquid phase was maintained at 1, while the temperature and the composition of the system was varied using a map function until all lines of twofold saturation were delineated, terminating either at a compositional axis (either Cr or Mo) or a ternary eutectic point. The position of these lines is crucial, as they separate the different regimes of primary solidification as a function of nominal composition. Sometimes referred to as monovariant eutectic lines, these thermodynamic features also dictate how liquid composition will vary once primary solidification is complete. The Fe-Data thermodynamic database[39] was used for the Fe-based alloy calculations, as the data contained in this database can include elements such as Mn, Si, and Cu which are unavailable in the Ni-Data database. The following phases were allowed to contribute to the simulation: liquid, γ (fcc), δ (bcc), σ (bct), P (orthorhombic, Ni-Data only), and NiMo (Ni-Data only).

As experimentally shown previously, microstructural development of these alloys is driven by the segregation of Mo during solidification; as such, describing the behavior of Mo during solidification is of central importance. The variation in Cr and Mo content in the liquid (*i.e.,* the solidification path) for each alloy was calculated with the ternary analog of the Scheil equation that was first proposed by Mehrabian and Flemings[43] as

$$C_{l,\mathrm{Mo}} = C_{0,\mathrm{Mo}} \left(\frac{C_{1,\mathrm{Cr}}}{C_{0,\mathrm{Cr}}} \right)^{\frac{k_{\mathrm{Mo}} - 1}{k_{\mathrm{Cr}-1}}} \qquad [1]$$

where $C_{l,\mathrm{i}}$ = concentration in liquid of element i, $C_{0,\mathrm{i}}$ = nominal concentration of element i, and k_{i} = partition coefficient for element i.

This is based on the same assumptions as used in the Scheil equation: dendrite tip undercooling and solid-state diffusion of each solute is negligible, diffusion is infinitely fast in the liquid, and thermodynamic equilibrium is maintained at the solid/liquid interface. These assumptions are reasonable considering the solidification conditions studied here are not expected to promote significant dendrite tip undercooling and the diffusivity of Mo in γ-austenite has been shown to be insignificant in very similar alloy systems processed under nearly identical conditions.[3] For multicomponent systems with small amounts of several alloying elements, it is assumed that their effect on solidification behavior can be accounted for by the position of the lines of twofold saturation in the multicomponent

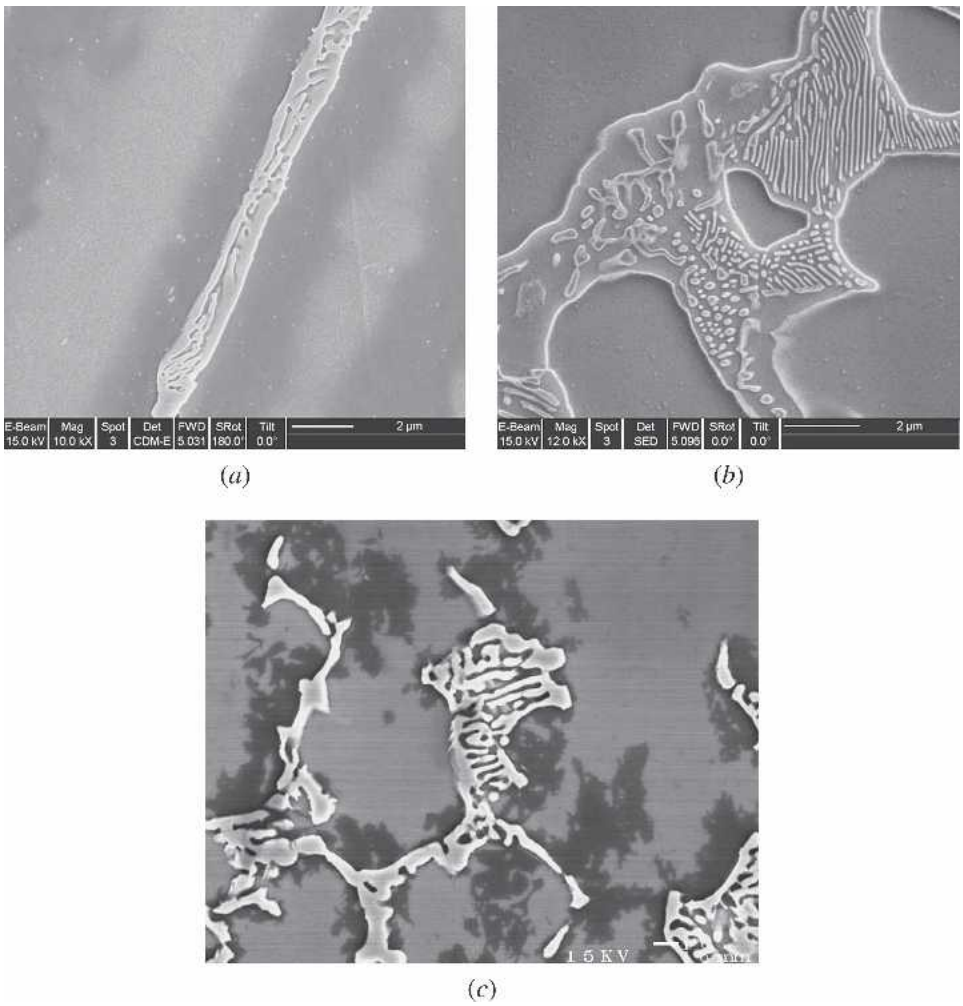

Fig. 5—Comparison of eutectic morphologies observed in a scanning electron microscope for gas tungsten arc weld specimens: (*a*) AL-6XN exhibiting elongated islands with eutectic, (*b*) Fe-base alloy 1 showing a eutectic morphology similar to that observed in the DTA specimen on the same material, (*c*) Ni-base alloy 3 with a distinct eutectic appearance involving blocky intermetallic islands in a γ matrix. All samples electrolytically etched with 60 pct HNO_3/40 pct H_2O mixture.

Table III. Chemical Composition of Second Phase and Average Eutectic for DTA Specimens (Standard Deviation is Expressed in Parentheses)

Material	Feature	Mo	Cr	Ni	Fe
AL-6XN	σ	17.1 (1.1)	29.2 (1.1)	12.9 (1.1)	38.1 (0.7)
	γ/σ average	14.9 (0.4)	27.0 (0.3)	15.5 (0.3)	40.6 (0.7)
Alloy 1	σ	21.1 (1.8)	25.9 (1.6)	15.3 (1.9)	37.5 (2.1)
	γ/σ average	18.6 (0.7)	23.8 (0.3)	18.5 (0.4)	40.0 (0.8)
	GTA weld γ/σ average	18.5 (1.0)	23.3 (0.6)	19.0 (0.8)	39.9 (1.0)
Alloy 2	no second phase	NA	NA	NA	NA
	no eutectic	NA	NA	NA	NA
Alloy 3	P	47.2 (0.4)	21.3 (0.9)	30.7 (1.9)	NA
	γ/P average	33.3 (1.0)	20.1 (0.3)	45.4 (1.5)	NA
	GTA weld γ/P average	33.4 (2.5)	20.9 (0.1)	45.4 (2.7)	NA

*NA = not available.

liquidus projection and, therefore, need not be included directly in the solidification path calculation (*i.e.*, the effect of these higher order elements on solidification is to change the position of the monovariant eutectic lines).[40]

The direction of the primary solidification path is determined by k_{Mo} and k_{Cr}, which are partition coefficients that govern solute redistribution during solidification and were experimentally measured in Section III. The primary

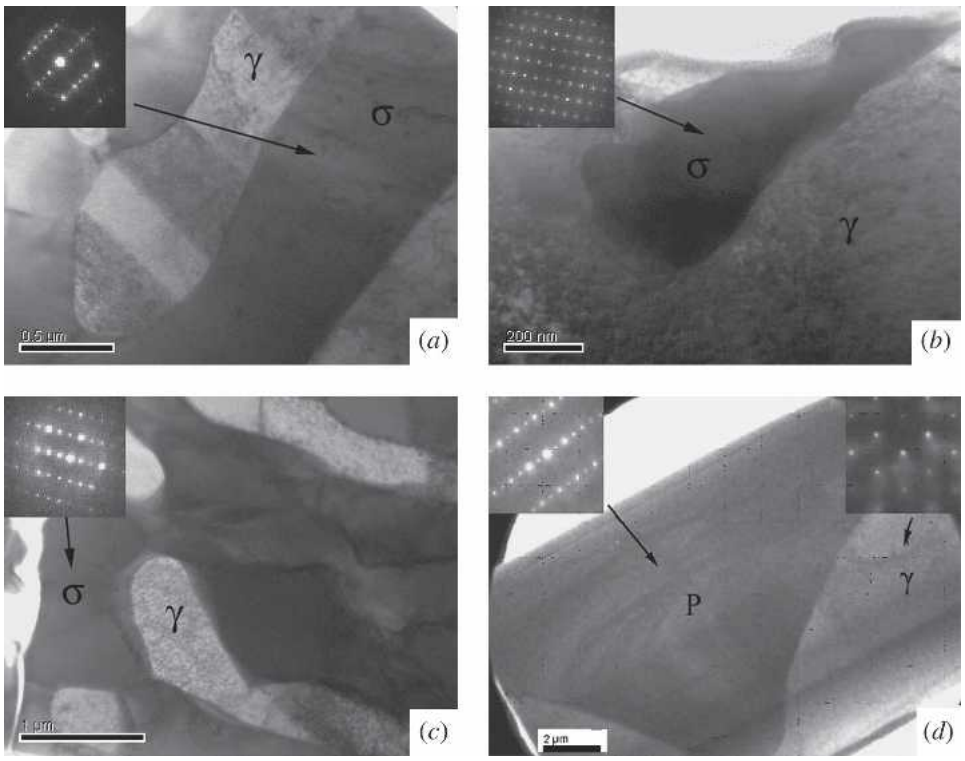

Fig. 6—Bright-field TEM images of the eutectic constituents with selected area diffraction patterns identifying intermetallic phases: (*a*) AL6XN DTA specimen oriented at a [-1, -1, 3] zone axis for σ, (*b*) AL6XN GTA weld specimen oriented at a [1, 1, 0] zone axis for σ, (*c*) alloy 1 DTA specimen oriented at a [2, 1, 2] zone axis for σ, and (*d*) alloy 3 oriented at a [-1, 0, 3] zone axis for P (sample was previously tilted to a [1, 1, 0] zone axis for γ, shown in the upper right of this figure).

solidification paths for the four alloys in this study were calculated using Eq. [1], using experimentally measured partition coefficient values (shown in Table IV) as constants. The result of the combination of the appropriate liquidus projection with the corresponding solidification path provides an interpretation of the solidification sequence of each alloy.

The amount of eutectic that is expected to form can also be determined based on the concentration of Mo in the liquid according to the same model:[43]

$$f_e = \left(\frac{C_{e,\mathrm{Mo}}}{C_{0,\mathrm{Mo}}}\right)^{\frac{1}{k_{\mathrm{Mo}} - 1}} \qquad [2]$$

where f_e is the fraction eutectic formed, $C_{e,\mathrm{Mo}}$ is the eutectic Mo concentration, $C_{0,\mathrm{Mo}}$ is the nominal Mo concentration, and k_{Mo} is the partition coefficient.

As a check on the consistency of the experimental data, Table V compares experimentally measured and calculated amounts of eutectic constituent observed in each alloy. The calculated values were determined by using the measured values of nominal Mo concentration (Table I), eutectic Mo concentration (Table III), and Mo distribution coefficients (Table IV) in Eq. [2]. The reasonable agreement between measured and calculated amounts of eutectic constituents provides confidence in the measured values of k and C_e. Also shown for comparison is the amount of eutectic constituent predicted from the Scheil module available in Thermo-Calc, which has the ability to account for variations in partition coefficient with decreasing temperature. Surprisingly, this method significantly overpredicts the amount of eutectic constituent for each alloy. Inspection of the calculations indicates this is most likely due to the disparity between calculated and measured eutectic compositions (C_e) for each alloy (Table VI), as little variation in k_{Mo} was observed between calculation and experiment. While the difference between measured and calculated C_e values is merely a few weight percent, the significant impact on the fraction eutectic (f_e) prediction demonstrates the sensitivity of f_e to variations in eutectic composition relative to the nominal. The following sections address this predictive inaccuracy directly and modifications to the liquidus projections are proposed to improve the thermodynamic description of the microstructural development of this class of materials.

B. *Ni-Based Alloys*

A multicomponent liquidus projection used to describe the solidification behavior of alloys 2 and 3 is shown in Figure 9(a) (based on the Ni-Cr-Mo ternary system but with appropriate additions of Fe, N, and C). Previous results have shown that the presence of other elements in even small quantities can significantly affect the position of phase boundaries on the liquidus projection.[40] Thus, the presence of Fe, N, and C were included in the calculations. The nominal composition of each alloy is indicated by the dot at the beginning of the calculated solidification paths, which extend sharply upward to the monovariant eutectic lines on

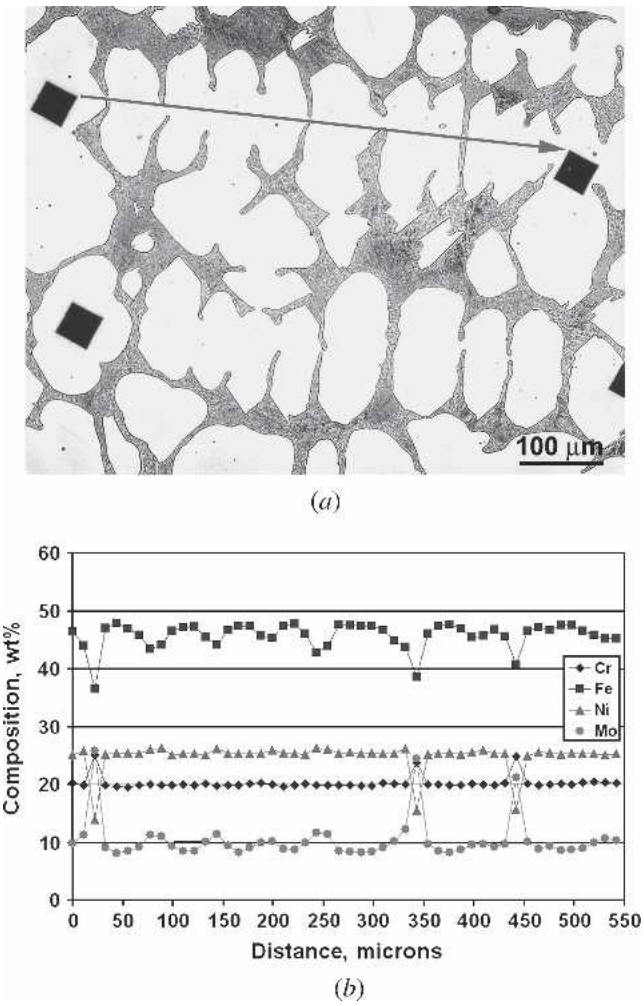

Fig. 7—EPMA line scan for DTA specimen for Fe-base alloy 1: (*a*) line scan extends across dendritic structure bounded by microhardness indentations; and (*b*) resulting chemical distribution data as a function of distance across the dendritic structure for (top to bottom) Fe, Ni, Cr, and Mo. The minima in Mo content correspond to dendrite cores (indicated by the arrows), while local maxima correspond to interdendritic regions.

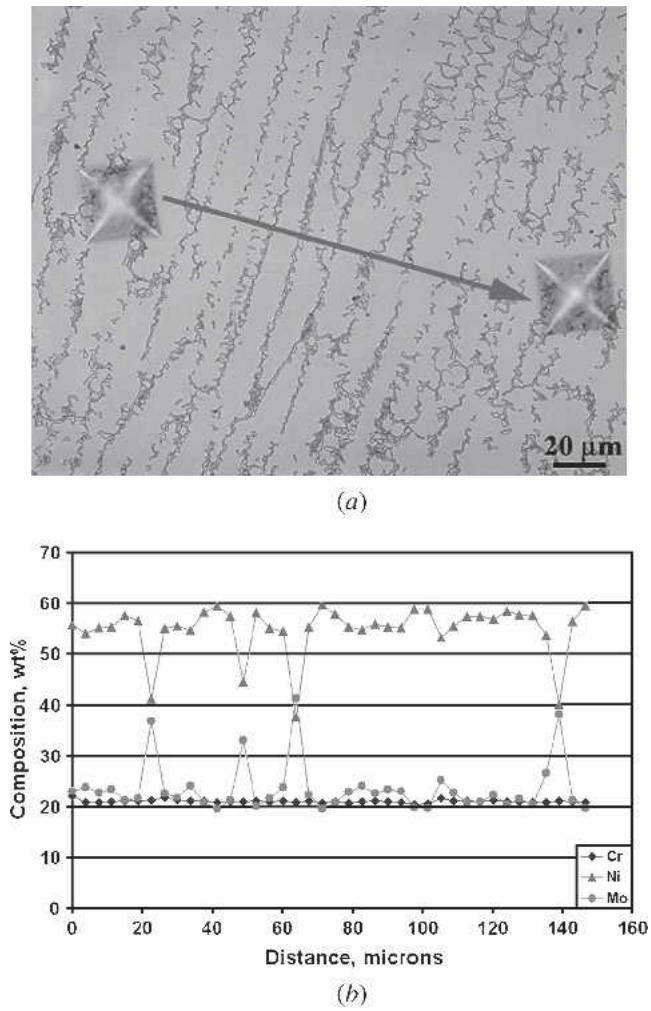

Fig. 8—EPMA line scan for GTA-welded specimen for Ni-base alloy 3: (*a*) Line scan extends across dendritic structure bounded by microhardness indentations; and (*b*) resulting chemical distribution data as a function of distance across the dendritic structure for (top to bottom) Ni, Mo, and Cr. The minima in Mo content correspond to dendrite cores (indicated by the arrows) while local maxima correspond to interdendritic regions.

the diagram as solidification proceeds. The nearly vertical character of these solidification paths are dictated both by the propensity of Mo to segregate to the liquid and the lack of significant Cr segregation to the liquid during γ solidification, a behavior exhibited by both alloys 2 and 3. For alloy 2, the solidification path tracks the liquid composition through the primary γ phase field to the line of twofold saturation between γ and σ. At this juncture, the liquid composition is expected to briefly follow the γ/σ monovariant eutectic line until the local minimum temperature is reached at the γ-σ-P ternary eutectic where solidification terminates. Thus, the expected solidification sequence for alloy 2 under nonequilibrium conditions is $L \rightarrow L + \gamma \rightarrow L + \gamma + \sigma \rightarrow L + \gamma + \sigma + P \rightarrow \gamma + \sigma + P$. Conversely, the higher Mo content of alloy 3 causes the primary γ solidification path to intersect the γ/P monovariant eutectic line instead of γ/σ, despite having the same nominal Cr content as alloy 2. The expected solidification sequence for alloy 3 is therefore $L \rightarrow L + \gamma \rightarrow L + \gamma + P \rightarrow L + \gamma + P + \sigma \rightarrow \gamma + P + \sigma$.

Alloy 2 exhibits only single-phase γ solidification ($L \rightarrow L + \gamma \rightarrow \gamma$) in both DTA and weld microstructures, indicating that solidification terminated before liquid Mo enrichment could induce γ/σ eutectic formation. Using the value of Mo concentration in the liquid at the intersection of the primary solidification path and twofold saturation as C_e in Eq. [2] indicates that only 0.01 wt pct γ/σ eutectic constituent would form under ideal nonequilibrium conditions (Table V), and as such, the absence of a eutectic constituent is only a very minor departure from this value. Thus, any small deviation from the ideal nonequilibrium case, such as backdiffusion, dendrite tip undercooling, or *k*-value variability, could account for the lack of a eutectic constituent in the microstructure.

The observed solidification sequence for alloy 3 is partially consistent with the one shown in Figure 9(a) in that primary $L \rightarrow L + \gamma$ solidification is directly followed by the $L + \gamma \rightarrow L + \gamma + P$ eutectic reaction. Figure 9 indicates that, after this binary-type eutectic reaction, solidification will terminate by formation of the γ/P/σ constituent.

Table IV. Elemental Partition Data Measured Using EPMA (Standard Deviation is Expressed in Parentheses; All Values are Expressed in Weight Percent)

Material	Quantity	Mo	Cr	Ni	Fe
AL-6XN	Nominal	6.1	21.6	24.2	46.8
	DTA dendrite core	4.8 (0.4)	20.5 (0.7)	24.0 (0.2)	49.4 (0.8)
	GTA weld dendrite core	4.7 (0.2)	21.0 (0.2)	24.3 (0.1)	49.0 (0.6)
	DTA *k* value	0.79 (0.07)	0.95 (0.03)	0.99 (0.01)	1.06 (0.02)
	GTA weld *k* value	0.77 (0.03)	0.97 (0.01)	1.00 (0.00)	1.05 (0.01)
Alloy 1	Nominal	12.4	20.1	23.9	43.6
	DTA dendrite core	8.4 (0.2)	20.0 (0.2)	25.3 (0.1)	47.4 (0.3)
	GTA weld dendrite core	8.8 (0.3)	20.0 (0.3)	25.1 (0.1)	46.5 (0.5)
	DTA *k* value	0.68 (0.02)	1.00 (0.01)	1.06 (0.00)	1.09 (0.01)
	GTA weld *k* value	0.71 (0.02)	1.00 (0.02)	1.05 (0.00)	1.07 (0.01)
Alloy 2	Nominal	12.1	20.6	66.9	NA*
	DTA dendrite core	9.6 (0.2)	20.5 (0.2)	70.1 (0.2)	NA
	GTA weld dendrite core	10.1 (0.2)	20.4 (0.3)	69.0 (0.5)	NA
	DTA *k* value	0.79 (0.02)	1.00 (0.01)	1.05 (0.00)	NA
	GTA weld *k* value	0.83 (0.02)	0.99 (0.01)	1.03 (0.01)	NA
Alloy 3	Nominal	24.3	20.2	54.5	NA
	DTA dendrite core	19.8 (1.1)	20.7 (0.4)	58.6 (1.2)	NA
	GTA weld dendrite core	19.9 (0.5)	20.7 (0.2)	59.0 (0.8)	NA
	DTA *k* value	0.81 (0.05)	1.02 (0.02)	1.08 (0.02)	NA
	GTA weld *k* value	0.82 (0.02)	1.02 (0.01)	1.08 (0.01)	NA

*NA = not available.

Table V. Comparison of Experimentally Measured Weight Percent Eutectic Data (Weight Fraction Eutectic ×100) and Calculated Values Based on Experimental Measurements (Thermo-Calc Scheil Module Also Used for Comparison)

Material	Sample	Experimental	Calculation with Measured Values of $C_{e,\mathrm{Mo}}, C_{0,\mathrm{Mo}}, k_{\mathrm{Mo}}$	Thermo-Calc Scheil Module (k_{Mo} Variable with T)
AL6XN	DTA	2.8	1.7	12
	Weld	1.1		
Alloy 1	DTA	27	26	69
	Weld	31		
Alloy 2	DTA	0.0	0.01*	2.7
	Weld	0.0		
Alloy 3	DTA	18	17	38
	Weld	23		

*Calculated $C_{e,\mathrm{Mo}}$ and k_{Mo} used because no eutectic was experimental observed.

However, only the binary-type γ/P eutectic constituent was observed. In addition, use of the Mo concentration at the intersection of the primary solidification path and γ/P eutectic line as C_e in Eq. [2] overpredicts the amount of γ/P eutectic as 33 wt pct (compared to measured value of 17 vol pct). The measured eutectic composition of the γ/P constituent for alloy 3 from Table III is shown in Figure 9(b). It is recognized that calculations for *weight* percent eutectic are being compared to direct measurements of *volume* percent eutectic and that a correction factor is normally required to account for differing densities of γ and σ. However, powder diffraction files available from the International Center for Diffraction Data indicate the densities of γ (7.950 Mg/m^3)[44] and σ (8.488 Mg/m^3)[45] are similar enough to justify omission of such a factor.

These observations suggest that (1) the location of the γ/P eutectic line should be shifted to higher Mo (and slightly higher Cr) concentrations and (2) the direction of decreasing temperature on the γ/P eutectic line may need to be reversed (this reversed direction would account for lack of the ternary eutectic γ/P/σ constituent). Each of these changes would bring the proposed liquidus projection in line with the observed solidification sequence and corresponding microstructure. These changes are shown in Figure 9(b), in which the adjoining eutectic lines between γ/P, P/σ, and γ/σ have been slightly relocated by shifting the calculated intersection point of the primary solidification path and γ/P eutectic line to the measured eutectic Mo and Cr concentrations (shown in Table III for alloy 3). The direction of decreasing temperature on the γ/P line was also reversed. It should be noted that these changes represent only an approximation based on experimental observations, but should provide a slight improvement in accuracy over the original liquidus projection shown in Figure 9(a). Note that this shift would also result in even less eutectic constituent forming in alloy 2, which is again consistent with

Table VI. Comparison of Calculated and Experimentally Measured Average Eutectic Compositions (All Values in Weight Percent)

Material	Source	Mo	Cr	Ni	Fe
AL-6XN	Scheil module (variable k)	12.7	26.4	21.6	37.9
	Calculation nominal composition	9.4	23.4	20.4	46.8
	Experiment and shifted diagrams	14.9 (0.4)	27.0 (0.3)	15.5 (0.3)	40.6 (0.7)
Alloy 1	Scheil module (variable k)	13.7	20.7	23.1	42.5
	Calculation nominal composition	13.6	20.0	22.6	45.0
	Experiment	18.6 (0.7)	23.8 (0.3)	18.5 (0.4)	40.0 (0.8)
Alloy 2	Scheil module (variable k)	26.4	26.9	46.7	—
	Calculation nominal composition	29.0	20.6	50.4	—
	Experiment	NA	NA	NA	—
Alloy 3	Scheil module (variable k)	29.0	21.2	49.8	—
	Calculation nominal composition	30.0	19.7	50.3	—
	Experiment	33.3 (2.5)	20.1 (0.3)	45.4 (1.5)	—

experimental observations. (The calculated solidification path should ideally intersect the measured eutectic composition in Figure 9(a), but a slight discrepancy is observed. This slight discrepancy is most likely caused by slight changes in k_{Cr} or k_{Mo} during solidification or experimental error of the eutectic composition measurements.)

C. *Fe-Based Alloys*

Multicomponent liquidus projections based on the nominal compositions of AL-6XN and alloy 1 are shown with their primary solidification paths in Figures 10(a) and (b), respectively. As mentioned previously, small changes in the amount of other alloying additions can have a significant effect on the position of phase boundaries on the liquidus projection.[40] Since some of these differences are appreciable between AL-6XN and alloy 1, separate projections are considered for each alloy. For AL-6XN (Figure 10(a)), the nominal composition lies in the primary γ-phase field and Mo enrichment of the liquid is expected to cause the primary solidification path to intersect the γ/δ boundary. The corresponding solidification sequence is therefore $L \rightarrow L + \gamma \rightarrow L + \gamma + \delta \rightarrow L + \gamma + \delta + \sigma \rightarrow L + \gamma + \sigma \rightarrow \gamma + \delta + \sigma$. This conflicts with the experimentally observed sequence ($L \rightarrow L + \gamma \rightarrow L + \gamma + \sigma \rightarrow \gamma + \sigma$) both in the first intermetallic to form (σ instead of δ) and in the absence of the $\gamma/\delta/\sigma$ ternary eutectic.

The experimentally measured γ/σ eutectic composition is also shown in Figure 10(a). As with the Ni base alloys, the calculated intersection of the primary solidification path and eutectic line also underestimate the eutectic composition. This can partially be explained by an added factor, which also must be taken into account for these alloys with high Fe content. The liquid Fe content can change appreciably during solidification and affect the position of the eutectic lines. For example, although the nominal Fe content of AL6XN is 46.8 wt pct, the EPMA data provided in Table III indicate that the Fe content in the liquid at the eutectic reaction is reduced to approximately 40.6 wt pct. This is consistent with the experimental k values for Fe presented in Table IV that are greater than unity, which indicate that Fe will segregate to the solid during solidification and lead to Fe depletion in the liquid. Thus, the eutectic lines are not truly stationary in a quaternary or higher order alloy, but are expected to shift as the concentration of other alloying elements in the liquid changes.

In order to estimate the expected magnitude of this shift, Figure 10(a) shows a recalculated liquidus projection at the measured eutectic Fe content of 40.6 wt pct. Note that the correct solidification sequence of $L \rightarrow L + \gamma \rightarrow L + \gamma + \sigma \rightarrow \gamma + \sigma$ is now predicted. The recalculation also resulted in a change of direction of decreasing temperature along the γ/σ line. With 46.8 wt pct Fe, the direction of decreasing temperature is away from the ternary eutectic point everywhere along the γ/σ line as shown. A reduction in the Fe content to 40.6 wt pct resulted in a peak temperature appearing on the γ/σ line at about 20 wt pct Mo. Below this point, the direction of decreasing temperature was toward the ternary eutectic point, while above this point, it was away from the ternary eutectic point. However, this indicates that the $\gamma/\sigma/\delta$ ternary eutectic constituent would form in AL6XN, but this is not observed experimentally. Thus, the direction of decreasing temperature is shown pointed away from the ternary eutectic point along the entire length of the γ/σ line. Last, the adjoining eutectic lines between γ/δ, δ/σ, and γ/σ for the 40.6 wt pct Fe projection have been slightly relocated by shifting the calculated intersection point of the primary solidification path and γ/σ eutectic line to the measured eutectic Mo and Cr concentrations (shown in Table III for AL6XN).

Figure 10(b) shows similar results for alloy 1 and the same observations are apparent. (1) The position of the eutectic lines at the nominal Fe content of 43.6 wt pct do not accurately predict the observed solidification sequence. (2) The correct sequence can be obtained by recalculating the positions at the observed eutectic Fe content of 40 wt pct while maintaining the direction of decreasing temperature. (3) The calculated intersection of the primary solidification path and eutectic line is underestimated in comparison to the experimental value. There is also a larger discrepancy between the solidification path and measured eutectic compositions, since these two should meet. This could possibly be caused by a reduction in k_{Cr} during solidification, a factor which is not accounted for in the constant k_{Cr} value used in the calculation. Note that the Cr concentration at the eutectic point for alloy 1 (Table III) is slightly higher than the nominal alloy Cr concentration (Table I), which indeed suggests that k_{Cr} is decreasing during solidification. As with

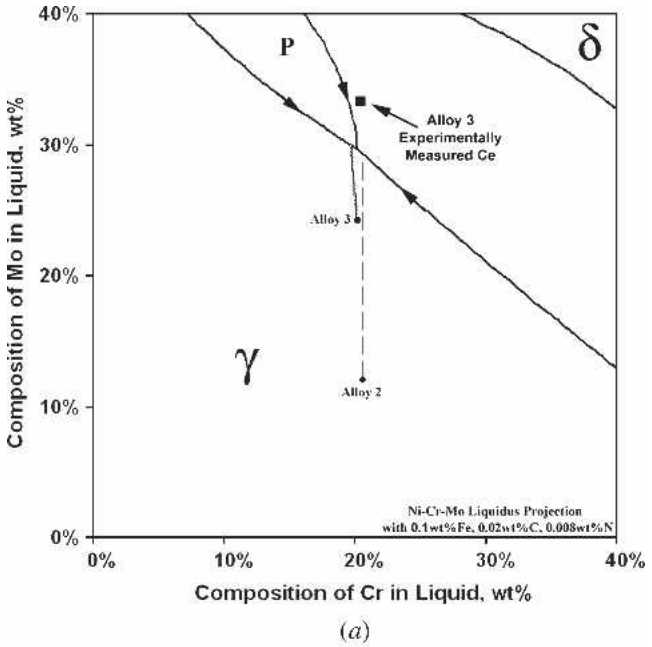

(*a*)

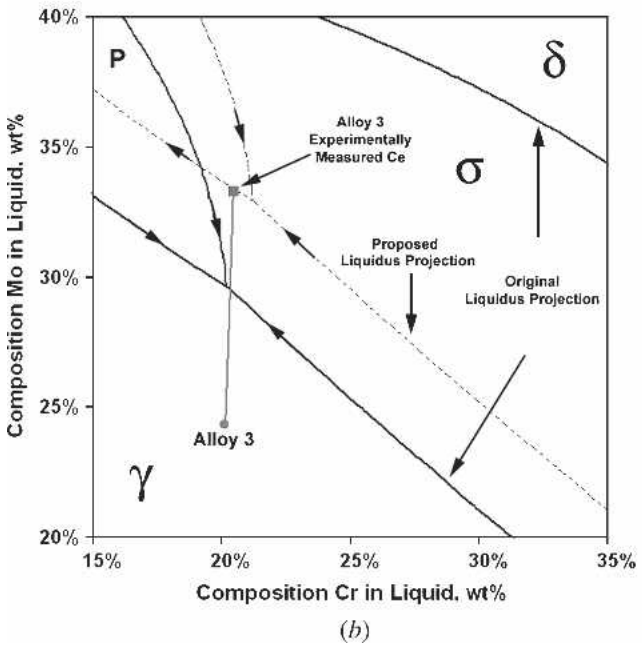

(*b*)

Fig. 9—Solidification simulation for Ni-Cr-Mo ternary alloys 2 and 3. (*a*) multicomponent liquidus projection based on the NiCrMo system with constant additions of 0.1 wt pct Fe, 0.02 wt pct C, and 0.008 wt pct N. The arrowheads on the lines of twofold saturation indicate their slope with decreasing temperature. (*b*) A minor shift in both Cr and Mo is required for the intersection of the primary solidification path for alloy 3 and monovariant γ/P eutectic line to coincide with the experimentally observed eutectic composition, Ce.

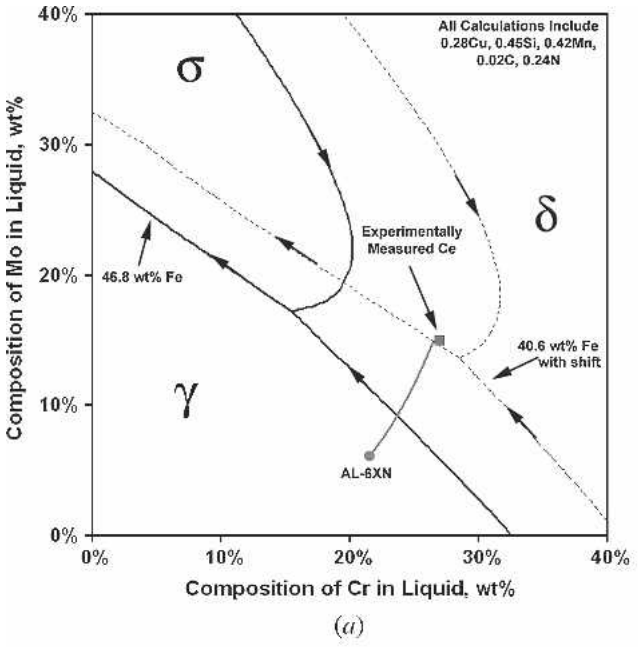

(*a*)

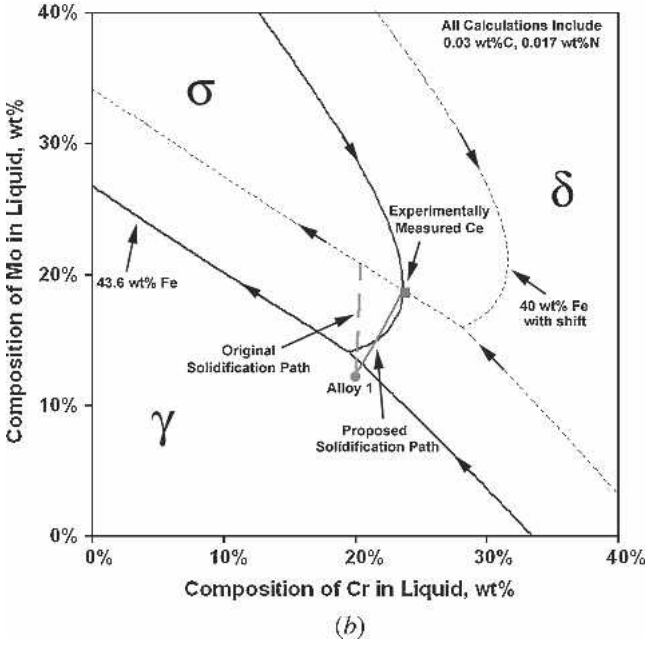

(*b*)

Fig. 10—(*a*) Solidification simulation of AL-6XN that includes the exact nominal composition of Fe, C, N, Mn, Si, and Cu, along with Ni, Cr, and Mo. A shifted projection for 40.6 wt pct Fe is superimposed to represent the partitioning of Fe to the liquid during solidification. (*b*) Solidification simulation for alloy 1 that uses the full nominal composition of the alloy, including exact composition of Fe, C, and N. A shifted projection for 40 wt pct Fe is superimposed to improve the description of alloy behavior. For both diagrams, the arrowheads on the lines of twofold saturation indicate their slope with decreasing temperature.

the previous projections, the best estimate of the position of the phase boundary lines is provided by shifting the calculated intersection point of the primary solidification path and γ/σ eutectic line (for 40 wt pct Fe) to the measured eutectic Mo and Cr concentrations. As with Figure 9, the projections shown in Figure 10 can only be considered approximate, but should be more accurate than those originally considered by the initial calculations.

The information presented here provides some useful insight into microstructural control of these alloys. For example, as previously indicated, Ni base alloys are often used for filler metals when joining Fe base SASS alloys. The extent of microsegregation and the type/amount of secondary phases in the fusion zone are expected to affect both corrosion performance and mechanical properties.

Recent results[46] have also shown that fusion zone solidification cracking susceptibility of these alloys is strongly affected by the type and amount of eutectic constituent that forms in the weld during solidification. The data presented here indicate that solid-state diffusion is not significant under the range of cooling rate conditions considered (recall that results from slow cooling rate DTA samples were similar to those of higher cooling rate GTA samples). In view of this, the extent of microsegregation can be assessed directly from the k values, while the amount of eutectic constituent is controlled by C_0, C_e, and k. Comparison between Ni and Fe base alloys at similar Mo levels (*i.e.*, alloys 1 and 2) indicate that Mo segregation will be slightly greater in Fe base alloys. This trend has been observed in actual dissimilar welds between AL6XN and Ni base filler metals and is attributed to the reduced solubility of Mo in γ that occurs with Fe additions.[3] The Ni base alloys will also form less eutectic constituent during solidification, which is generally associated with better weldability, corrosion resistance, and mechanical properties. The results presented here indicate this can be attributed to slightly higher k_{Mo} values and higher $C_{e,\mathrm{Mo}}$ values for the Ni base alloys. This type of information may be useful in future alloy development activities.

V. CONCLUSIONS

The solidification behavior of several Ni-Cr-Mo and Fe-Ni-Cr-Mo alloys was investigated with a combination of DTA and microstructural characterization techniques. The following conclusions can be drawn from this work.

1. The series of solidification reaction sequences for each alloy can be described as follows:

$$\text{AL-6XN: } L \rightarrow L + \gamma \rightarrow L + \gamma + \sigma \rightarrow \gamma + \sigma$$
$$\text{Alloy 1: } L \rightarrow L + \gamma \rightarrow L + \gamma + \sigma \rightarrow \gamma + \sigma$$
$$\text{Alloy 2: } L \rightarrow L + \gamma \rightarrow \gamma$$
$$\text{Alloy 3: } L \rightarrow L + \gamma \rightarrow L + \gamma + P \rightarrow \gamma + P$$

2. The segregation behavior of Mo has a strong influence on the microstructural development in the materials studied, as increases in nominal Mo content resulted in a concomitant increase in the amount of γ/σ and γ/P eutectic constituents.
3. The segregation behavior of Mo, Cr, Fe, and Ni was seen to be insensitive to cooling rate in the range of conditions studied here as no shift in behavior was observed between DTA samples ($<$0.2 °C/s) and autogenous arc welds on the same materials.
4. Multicomponent liquidus projections, which were originally calculated exclusively with the nominal composition of each alloy and subsequently slightly modified to account for experimental observations, have been proposed as an aid to understanding microstructural development in these alloys.

ACKNOWLEDGMENTS

This work was supported by the Office of Naval Research, under Contract No. N00014-00-1-0448. The authors also acknowledge the American Welding Society's support of this work through a Graduate Research Fellowship sponsored by the Navy Joining Center. The authors particularly thank Masashi Watanabe and David Ackland, Lehigh University, for their technical assistance. Sandia is a multiprogram laboratory operated by Sandia Corporation, a Lockheed Martin Company, for the United States Department of Energy's National Nuclear Security Administration under Contract No. DE-AC04-94AL85000.

REFERENCES

1. S.A. David, G.M. Goodwin, and D.N. Braski: *Welding Res. (Miami)*, 1979, vol. 58, pp. 330s-36s.
2. J.N. DuPont: *Weld. J. (Miami)*, 1999, vol. 78, pp. 253s-63s.
3. S.W. Banovic, J.N. DuPont, and A.R. Marder: *Sci. Technol. Weld. Joining*, 2002, vol. 7, pp. 374-83.
4. A. Garner: *Corrosion (Houston)*, 1979, vol. 35, pp. 108-14.
5. A. Garner: *Mater. Performance*, 1982, vol. 21, pp. 9-14.
6. M.B. Rockel and M. Renner: *Werkst. Korr.*, 1984, vol. 35, pp. 537-42.
7. P.I. Marshall and T.G. Gooch: *Corrosion (Houston)*, 1993, vol. 49, pp. 514-26.
8. A.H. Tuthill and R.E. Avery: *Welding Res. (Miami),* 1993, vol. 2, pp. 41-49.
9. A. Garner: *Met. Progr.,* 1985, vol. 127, pp. 31-32, 34-36.
10. T. Ogawa and T. Koseki: *Mater. Performance*, 1996, vol. 35, pp. 87-91.
11. J.W. Elmer, T.W. Eagar, and S.M. Allen: *Weldability Mater., Proc. Mater. Weldability Symp.*, Detroit, MI, ASM International, Materials Park, OH, 1990.
12. V.P. Kujanpaa and S.A. David: *Proceedings, 5th International Congress on Applications of Lasers and Electro-optics (ICALEO 86)*, IFS Publications, Kempston, Bedford, United Kingdom, 1987, pp. 63-69.
13. Y. Nakao, N. Kazutoshi, W.P. Zhang, and Y. Tamura: *Q. J. Jpn. Welding Soc.*, 1991, vol. 9, pp. 122-28.
14. Y. Nakao, K. Nishimoto, and W.P. Zhang: *Trans. Jpn. Welding Soc.*, 1988, vol. 19, pp. 100-06.
15. M.J. Perricone and J.N. DuPont: *6th Int. Conf. on Trends in Welding Research*, ASM INTERNATIONAL, Materials Park, OH, 2002.
16. M.J. Cieslak, T.J. Headley, and A.D. Romig, Jr.: *Metall. Trans. A*, 1986, vol. 17A, pp. 2035-47.
17. E. Gozlan, M. Bamberger, S.F. Dirnfeld, B. Prinz, and J. Klodt: *Mater. Sci. Eng.*, 1991, vol. A141, pp. 85-95.
18. E. Gozlan, S.F. Dirnfeld, M. Bamberger, J. Klodt, and B. Prinz: *Z. Metallkd.*, 1993, vol. 84, pp. 776-80.
19. J.A. Brooks and A.W. Thompson: *Int. Mater. Rev.*, 1991, vol. 36, pp. 16-44.
20. S. Atamert and J.E. King: *Acta Metall. Mater.*, 1991, vol. 39, pp. 273-85.
21. J.W. Elmer, S.M. Allen, and T.W. Eagar: *Metall. Trans. A*, 1989, vol. 20A, pp. 2117-31.
22. J.M. Vitek and S.A. David: in *The Metal Science of Joining*, M.J. Cieslak, J.H. Perepezko, S. Kang, and M.E.Glicksman, eds., Cincinnati, OH, 1992, pp. 115-22.
23. J.A. Brooks, M.I. Baskes, and F.A. Greulich: *Metall. Trans. A*, 1991, vol. 22A, pp. 915-26.
24. J.N. DuPont, C.V. Robino, and A.R. Marder: *Acta Mater.*, 1998, vol. 46, pp. 4781-90.
25. B. Sundman: *Rev. Alloys Modeling*, *Anales de Fisica*, *Ser. B*, 1990, vol. 86, pp. 69-82.
26. B. Sundman: *Thermo-Calc. [N]. 2001*, KTH, Stockholm, 1996.
27. N. Saunders: *Ni-Data Thermodynamic Database. [4.0]*, Thermotech, Ltd., Guildford, United Kingdom, 2000.
28. J.N. DuPont, C.V. Robino, J.R. Michael, M.R. Notis, and A.R. Marder: *Metall. Mater. Trans. A*, 1998, vol. 29A, pp. 2785-96.
29. J.N. DuPont: *Metall. Mater. Trans. A*, 1996, vol. 27A, pp. 3612-20.
30. M.J. Cieslak, T.J. Headley, T. Kollie, and A.D. Romig, Jr.: *Metall. Trans. A*, 1988, vol. 19A, pp. 2319-31.
31. M.J. Cieslak: *Welding Res. (Miami)*, 1991, vol. 70, pp. 49-56.
32. C.V. Robino, J.R. Michael, and M.J. Cieslak: *Sci. Technol. Welding Joining*, 1997, vol. 2, pp. 220-30.

33. G.A. Knorovsky, M.J. Cieslak, T.J. Headley, A.D. Romig, Jr., and W.F. Hammetter: *Metall. Trans. A*, 1989, vol. 20A, pp. 2149-58.
34. *ASTM International E562-02*, ASTM, West Conshohocken, PA, 2002.
35. K.F.J. Heinrich, A.D. Romig, Jr., and W.F. Chambers: *Microbeam Analysis*, Proceedings of the 21st Annual Conference of the Microbeam Analysis Society, Albuquerque, NM, 1986, A.D. Romig, Jr. and W.F. Chambers, eds., San Francisco Press, Inc., San Francisco, CA.
36. B. Weiss and R. Stickler: *Metall. Mater. Trans. A*, 1972, vol. 31A, p. 851.
37. M. Raghavan, R.R. Mueller, G.A. Vaughn, and S. Floreen: *Metall. Mater. Trans. A*, 1984, vol. 15A, pp. 783-92.
38. D.S. Bloom and N.J. Grant: *Trans. TMS-AIME,* 1954, pp. 261-68.
39. N. Saunders: *Fe-Data Thermodynamic Database. [3.0]*, ThermoTech Ltd., Guildford, United Kingdom, 2001.
40. M.J. Perricone, J.N. DuPont, and M.J. Cieslak: *Metall. Mater. Trans. A*, 2003, vol. 34A, pp. 1127-32.
41. K.P. Gupta: *Phase Diagrams of Ternary Nickel Alloys, Part I*, Indian Institute of Metals, Calcutta, 1990.
42. M.J. Perricone and J.N. DuPont: *Int. Conf. Joining of Advanced and Specialty Materials*, J.E. Indacochea and J.N.V. DuPont, eds., ASM INTERNATIONAL, Materials Park, OH, 2002.
43. R. Mehrabian and M.C. Flemings: *Metall. Trans.*, 1970, vol. 1, p. 455.
44. R. Pfoertsch: *Austenite, [PDF Card 33-0397]*, International Centre for Diffraction Data, 1982.
45. B. Duwez: *Sigma Phase, FeCrMo, [PDF Card 09-0050]*, International Centre for Diffraction, Newtown Square, PA, 1950.
46. J.N. DuPont, S.W. Banovic, and A.R. Marder: *Welding J.*, 2003, vol. 82, pp. 125s-35s.